ACTA UNIVERSITARIA
Multidisciplinary Scientific Journal

I VOLUMEN 32 I 2022 I

ISSN online 2007-9621
http://doi.org/10.15174/au.2022.3196

Study of the effects of vanadium and molybdenum on the microstructure of ductile iron (DI) and austempered ductile iron (ADI) and their corrosion resistance

Efecto del vanadio y molibdeno en la microestructura del hierro dúctil (DI) y el hierro dúctil austemperizado (ADI) y su resistencia a la corrosión

Victor H. Gutiérrez Pérez [1], Alejandro Cruz Ramírez [2], *Seydy L. Olvera Vázquez [1], Eduardo Colin García [3], Ricardo G. Sánchez Alvarado. [3], Miguel F. Delgado Pamanes [1] and Jorge E. Rivera Salinas

[1]Departamento de Formación Profesional Específica. Instituto Politécnico Nacional - Unidad Profesional Interdisciplinaria de Ingeniería campus Zacatecas (UPIIZ). Blvd. del Bote 202, Cerro del Gato, Ejido la Escondida, Ciudad Administrativa, Zacatecas, Zacatecas, México. 98160. Tel. 55 5729 6000. vhgutierrez@ipn.mx, *solverav@ipn.mx, mfdelgadop@ipn.mx.
[2]Departamento de Formación Básica Disciplinaria. Instituto Politécnico Nacional – Unidad Profesional Interdisciplinaria de Ingeniería campus Hidalgo (UPIIH). Carretera Pachuca - Actopan Kilómetro 1+500 Ciudad del Conocimiento y la Cultura, San Agustín Tlaxiaca, Hidalgo. 42162. Tel. 55 5729 6000. alcruzr@ipn.mx
[3]Departamento de Ingeniería en Metalurgia y Materiales, Instituto Politécnico Nacional, Escuela Superior de Ingeniería Química e Industrias Extractivas (ESIQIE). Av. Luis Enrique Erro S/N, Unidad Profesional Adolfo López Mateos, Zacatenco, Alcaldía Gustavo A. Madero, Ciudad de México. C.P. 07738. Tel. 55 5729 6000. metalurgista.eduardo@hotmail.com, risanchez@ipn.mx,
[4]Catedrático CONACyT – Departamento de Procesos de transformación. Centro de Investigación en Química Aplicada – CIQA. Blvd. Enrique Reyna Hermosillo No. 140. Saltillo, Coahuila México. C.P. 25294. Tel. 84 4438 9830. enrique.rivera@ciqa.edu.mx
*Autor de correspondencia

Abstract

Ductile iron (DI) can acquire various properties with the addition of alloying elements and through heat treatment. In this work, the effects of vanadium and molybdenum on the microstructure and corrosion resistance of DI and austempered ductile iron (ADI) were studied. Corrosion resistance was evaluated by potentiodynamic polarization techniques in 0.5 M H_2SO_4, 0.5 M NaCl, and 05 M NaOH as electrolyte. The ADI alloyed with vanadium presented an upper ausferritic microstructure consisting of broad ferrite needles, while the combination of vanadium and molybdenum allows obtaining a fine microstructure composed of ausferrite and thin needles of ferrite; this microstructure improves the corrosion resistance in NaCI and NaOH. The DI's showed corrosion due to the galvanic pair between the graphite nodule and the ferrite; however, a high amount of carbide increases the corrosion resistance in H_2SO_4.

Keywords: ADI; vanadium; molybdenum; microstructure; corrosion.

Resumen

El hierro dúctil (DI) puede modificar sus propiedades con la adición de elementos aleantes y tratamientos térmicos adecuados. En este trabajo se estudiaron los efectos del vanadio y molibdeno en la microestructura y resistencia a la corrosión del DI y el hierro dúctil austemperizado (ADI). La resistencia a la corrosión fue evaluada por la técnica de polarización potencio-dinámica en 0.5 M H_2SO_4, 0.5 M NaCl y 0.5 M NaOH como electrólito. El ADI aleado con vanadio presenta ausferrita gruesa formada por agujas gruesas de ferrita, mientras que la combinación de vanadio y molibdeno permite obtener una microestructura fina compuesta de ausferrita y agujas delgadas de ferrita; esta microestructura mejora la resistencia a la corrosión en NaCl y NaOH. El DI presenta corrosión debido al par galvánico entre los nódulos de grafito y la ferrita; sin embargo, la presencia de una gran cantidad de carburos incrementa su resistencia a la corrosión en H_2SO_4.

Palabras clave: ADI; vanadio; molibdeno; microestructura; corrosión.

Recibido: 12 de abril de 2021 Aceptado: 03 de noviembre de 2021 Publicado: 26 de enero de 2022

Cómo citar: Gutiérrez Pérez, V. H., Cruz Ramírez, A., Olvera Vázquez, S. L., Colin García, E., Sánchez Alvarado, R. G., Delgado Pamanes, M. F., & Rivera Salinas, J. E. (2022). Study of the effects of vanadium and molybdenum on the microstructure of ductile iron (DI) and austempered ductile iron (ADI) and their corrosion resistance. *Acta Universitaria 32*, e3196. doi. http://doi.org/10.15174.au.2022.3196

Introduction

Ductile iron (DI) can be cast into intricate shapes because of its excellent fluidity and relatively low melting point, and it can be alloyed for improvement of corrosion resistance and strength. Because of the excellent properties obtainable with this low–cost engineering material, ductile iron finds a wide variety of applications, for example, automotive and machine parts, tubes, and applications in environments that demand good corrosion resistance, such as water, soils acids, alkalis, saline solutions, organic compounds, and liquid metals (ASM International, 2009; Roy, 1988). DI can acquire various desirable mechanical properties and corrosion resistance with the addition of proper alloying elements and through heat treatment. Alloying elements can play a dominant role in the susceptibility of ductile iron to corrosion attacks. The alloying elements generally used to enhance the corrosion resistance of ductile cast iron include silicon, nickel, chromium, and copper. Other alloying elements used to a lesser extent are vanadium, titanium, and molybdenum (ASM International, 2009; Roy, 1988). On the other hand, through austempering heat treatment, the microstructure of ductile iron can be modified, so its microstructure is "ausferrite", which consists of ferrite (α) and high carbon austenite (γ_{HC}). The austempered ductile iron (ADI) obtained delivers twice the strength of conventional ductile iron for a given level of elongation, with exceptional wear and fatigue resistance (Brandenberg *et al.*, 2001). Intercritical heat treatments can also be performed on DI to increase the mechanical properties. Intercritical heat treatments can be applied to obtain microstructures of graphite nodules in a matrix of ferrite and austenite particles or graphite nodules in a matrix of ferrite and tempered martensite (Aristizabal *et al.*, 2012; Machado *et al.*, 2020). Corrosion behavior, like mechanical properties, is related to the alloy microstructure. A survey of the literature indicates that some attention has been paid to the corrosion resistance of DI and ADI mainly alloyed with nickel (Cheng-Hsun & Ming-Li, 2010; Minkoff, 1983; Yufu *et al.*, 2012). Also, it is well known that nickel is the most commonly used alloying element because it decreases primary carbide stability while increasing the finesses of pearlite, thus, increasing the strength of the iron (Minkoff, 1983). High-nickel ductile iron has been specified by the ASTM A439 standard for its resistance to heat and corrosion as well as for other special purposes (Yufu *et al.*, 2012). Experiments on the corrosion of cast irons and austempered chilled ductile iron containing nickel indicate that corrosion decreased with increasing nickel content (Hemanth, 2000; Rajagopal & Iwasaki, 1992).

The corrosion behavior of each group of cast iron is very different from that of other groups; however, in general, single phases such as ferrite and austenite tend to be less corrosion resistant than two-phase mixtures (e.g., pearlite and ausferrite) (ASM International, 1992). ADI austempered at low temperatures in the range from 250 °C to 330 °C allow obtaining a lower ausferritic microstructure, while high austempered temperatures (330 °C–450 °C) promote the formation of upper ausferritic microstructures, which consist of broad blades of isolated ferrite; this microstructure results in a high tensile toughness (Blackmore & Harding, 1984). The electrochemical behavior and corrosion resistance of ADI were evaluated by electrochemical techniques in sodium chloride solution. It has been shown that ADI containing an upper ausferritic microstructure attained higher corrosion resistance than an ADI with a lower ausferritic microstructure (Krawiec *et al.*, 2009). Molybdenum was found to contribute substantially towards improving the corrosion resistance of ductile iron, particularly in high silicon ductile irons (ASM International, 2009). Moreover, the nickel and molybdenum content combination of austempered chilled ductile iron, together with chilling and austempering, contribute to its superior corrosion resistance (Hemanth, 2000). The corrosion performance of conventional DI and ADI was evaluated to low sodium chloride concentrations (0.01 M and 0.05 M) by chronopotentiometry and potentiodynamic polarization techniques. Both samples appeared to have comparable corrosion attacks; however, the austempering heat treatment help in the stabilization of nodules improving its corrosion resistance for the corrosive media (Akinribide *et al.*, 2019).

The effects of the molybdenum addition on the microstructure, wear resistance, and corrosion resistance of carbidic austempered ductile iron (CADI) were studied. The corrosion resistance was evaluated by polarization curves in a 3.5 wt % NaCl solution. As the molybdenum content increased, the quantity of austenite and carbides increased, while the acicular ferrite became finer and corrosion resistance increased (Han *et al.*, 2015a). However, higher corrosion resistance of cast iron can be achieved not only by the addition of alloying elements but also by heat treatment (Gonzaga & Fernández, 2005). Vanadium enhances the graphite morphology and matrix structure in ductile iron. Besides this, vanadium can refine grains effectively and promote the formation of acicular ferrite; consequently, better properties are expected. Few published research articles about the vanadium effect on the corrosion behavior in ductile cast iron and austempered ductile iron are available. The present work aims to study the influence of vanadium on the relationship between microstructure and corrosion resistance of ductile iron and austempered ductile iron low alloyed with vanadium and vanadium–molybdenum by potentiodynamic polarization techniques in 0.5 M H_2SO_4, 0.5 M NaCl, and 0.5 M NaOH corrosive media.

Methods and Materials

Three cast alloys, identified as DI for the unalloyed ductile iron, DI-A for the ductile iron alloyed with 0.5 wt % V, and DI-B for the ductile iron alloyed with 0.5 wt % Mo and 0.49 wt % V, were produced in a 50 kg medium-frequency coreless induction furnace. The base iron was prepared with a mixture of 35 wt % low C and Mn steel, 30 wt % pig iron, and 35% cast iron scrap as the metallic charge. Table 1 shows the chemical composition of the base iron. High purity carbon riser, FeSi (75%), FeMo (62.83%), and FeV (75.34%) were used to adjust the chemical composition of the charge. All the materials were melted and homogenized at 1500 °C–1520 °C. The melt was nodulized with 1.5% nodulizing MgFeSi (45% Si, 8% Mg, 3.3% Ca, 3% Rare Earths) on the bottom of a preheated ladle (20 cm ID, 35 cm deep) covered with low carbon steel scrap at 1440 °C-1460 °C. After skimming the slag of the nodulized melt, 1.0% foundry grade FeSi (75% Si, 1% Ca, 0.9% Al, 1.1% Ba) was added by the ladle inoculation method, where the inoculant was added to the metal stream as it flowed from the nodulized ladle into a preheated pouring type shank ladle (21 cm ID, 20 cm deep).

Table 1. Chemical composition (wt. %) of the base iron.

Cast alloy	C	Si	Mn	P	S	Mg	Ni	Cr	Mo	V	Al	Cu
DI	2.43	0.98	0.27	0.02	0.028	0.001	0.01	0.11	0.005	0.01	0.01	0.03
DI-A	2.41	1.19	0.20	0.03	0.027	0.001	0.01	0.11	0.005	0.005	0.01	0.02
DI-B	2.38	1.46	0.25	0.03	0.019	0.001	0.01	0.13	0.005	0.01	0.03	0.04

Source: Authors' own elaboration.

Each of the three cast alloys were then poured at 1420 °C-1440 °C into three green sand molds to obtain plates of 120 mm x 40 mm and a thickness ranging from 25.4 mm to 4.23 mm by using the pattern shown in Figure 1.

ISSN online 2007-9621

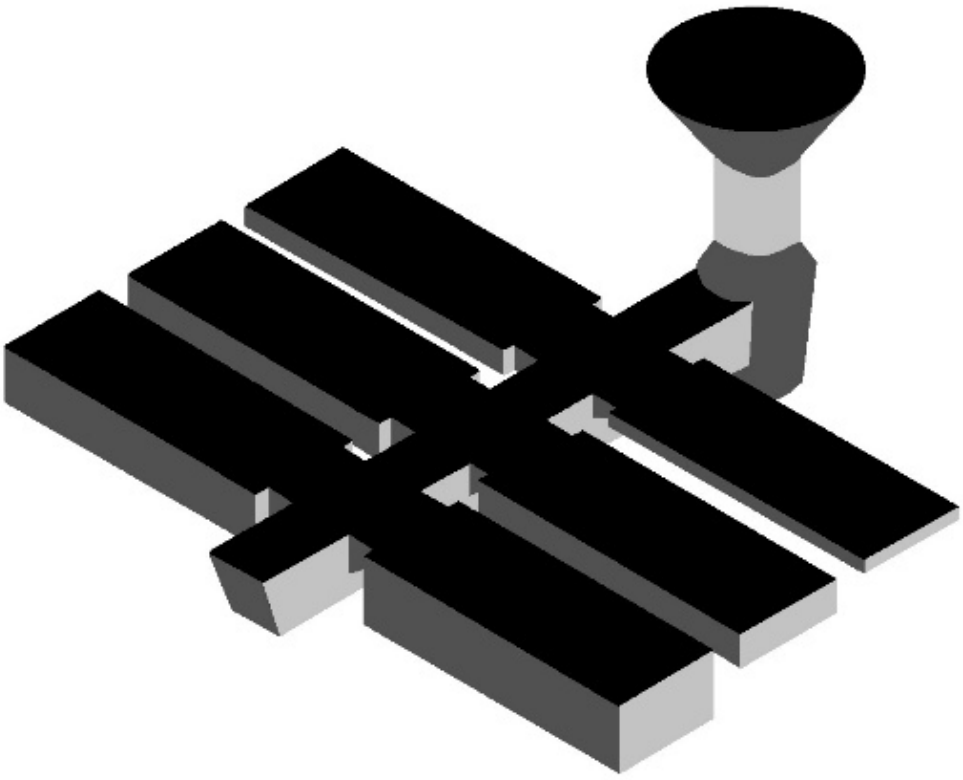

Figure 1. Pattern design with plates of six different thicknesses.
Source: Authors' own elaboration.

The nominal chemical composition in the castings was analyzed by an Oxford spark emission optic spectrograph. The reported values in Table 2 are the average of three measurements on each cast alloy. Carbon and sulfur content were determined by combustion analysis, using a Leco C/S analyzer.

Table 2. Chemical composition (wt. %) of the cast alloys.

Cast alloy	C	Si	Mn	P	S	Mg	Ni	Cr	Mo	V	Al	Cu	CE[1]
DI	3.43	2.41	0.30	0.02	0.019	0.037	0.01	0.10	0.005	0.01	0.02	0.06	4.24
DI-A	3.42	2.62	0.19	0.04	0.020	0.047	0.01	0.11	0.005	0.5	0.03	0.03	4.30
DI-B	3.40	2.89	0.23	0.03	0.014	0.046	0.01	0.13	0.50	0.49	0.04	0.06	4.37

[1]CE: Carbon equivalent. Balance Fe
Source: Authors' own elaboration.

Samples of the plate of 4.23 mm thick were used for heat treatment to evaluate the microstructural and corrosion behavior of the ductile iron and austempered ductile iron produced. The austempering heat treatment was as follows: the samples were austenitizing at 950 °C for 1 h; then, they were quenched in a salt bath (97.8% $NaNO_3$ and 2.2% Na_2CO_3) at 300 °C for 1 h, finally they were cooled down with water at room temperature.

Standard metallography techniques (mechanical grinding and polishing followed by etching with 2% nital) were employed to reveal the different microconstituents of the cast alloys. Optical microscopy was performed on polished and etched specimens by using an optical microscope Olympus PMG-3 model, the ASTM A 247 standard, and an image-analyzer with the software Image J version 4.1. The graphite morphology was rated for the nodule count by ASTM standard A 247 and average nodule size on the unetched samples. Phase volume fraction measurements, including nodule graphite, pearlite, ferrite, and carbides, were carried out using the image-analyzer with the software Image J version 4.1. Carbides were revealed by etching 2 min with a water solution of ammonium persulfate (10% vol) (Pedro & Dommarco, 2019). The optical microscopy measurements represent the average of eight different regions on each sample.

Before electrochemical measurements were carried out, DI and ADI samples were embedded in an epoxy resin to control the surface area. The samples were mechanically ground with silicon carbide emery papers down to 600 grit. The samples were ultrasonically rinsed in ethanol between each step. Corrosion behavior of the samples was evaluated by anodic potentiodynamic polarization test in a Potentiostat-Galvanostat AutoPG-UAM equipped with a conventional three-electrode system electrochemical workshop with the DI and ADI samples as the working electrode, graphite as the counter electrode, and a saturated calomel electrode as the reference. All tests were conducted at 25 °C, at molarity held constant in 0.5 M of sulphuric acid, sodium hydroxide, and sodium chloride as corrosive media, and tests were repeated for reproducibility. The electrode potential sweep was raised from -0.25 V to +0.25 V from open circuit potential (OCP), with the scanning rate of 1 mV/s. Corrosion current density values were obtained by the Tafel extrapolation method (McCafferty, 2005; Stern & Geary, 1957).

Results and Discussion

The nominal chemical composition analyzed in the castings is shown in Table 2. The equivalent carbon was hypoeutectic for heats DI and DI-A and hypereutectic for heat DI-B. The silicon content was high to improve graphitization under the high cooling rates imposed by the low thickness of the casting plate used. The residual magnesium content of 0.032%, on average, was obtained in heats for an adequate nodule formation. The amount of vanadium and molybdenum was set at 0.5 wt % for heats DI-A and DI-B.

Figure 2 shows the unetched microstructure of cast alloys manufactured. A homogeneous distribution of spheroidal graphite for the cast alloys with a high nodule count is observed. The largest nodules in low amounts are observed for the cast alloy DI, while the smallest nodules belong to the low alloyed ductile irons (DI-A and DI-B).

ISSN online 2007-9621

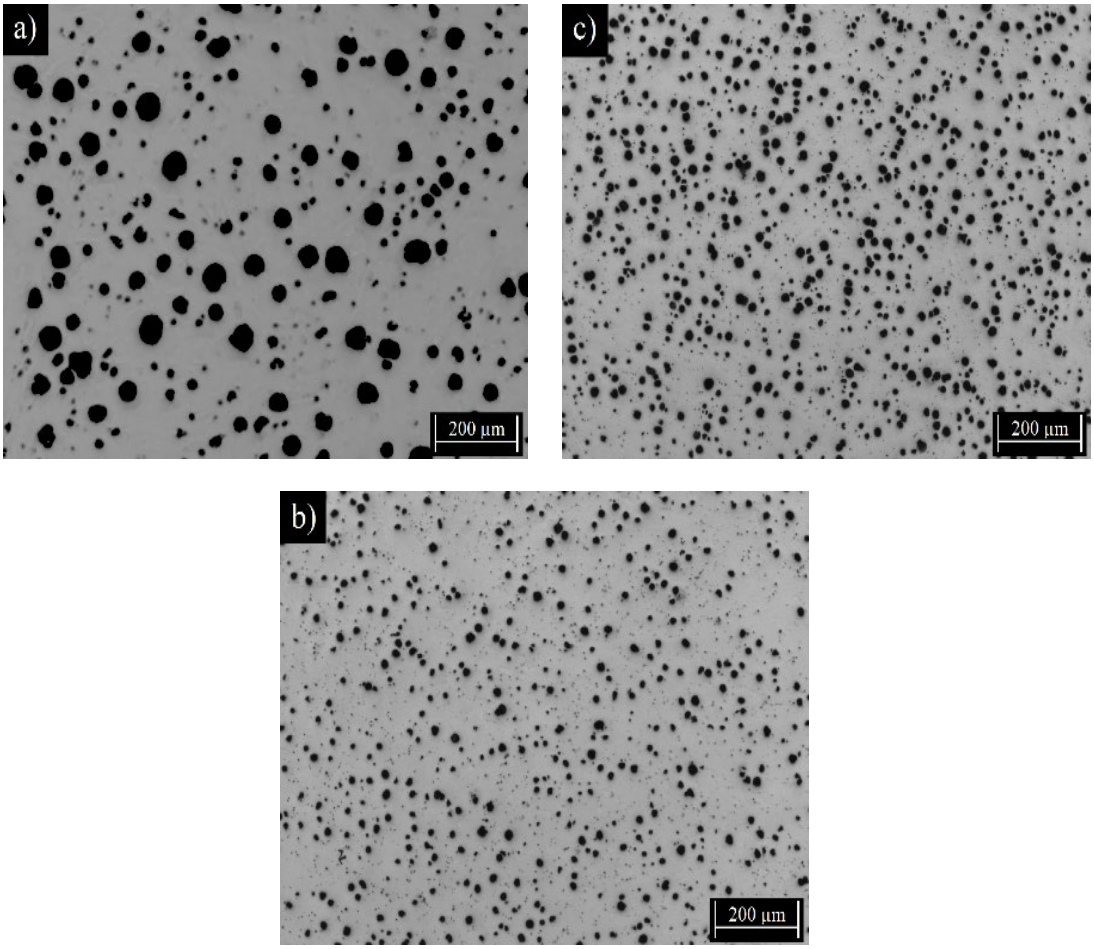

Figure 2. Unetched microstructure of cast alloys: a) DI, b) DI-A, and c) DI-B.
Source: Authors' own elaboration.

ISSN online 2007-9621

Figure 3 shows the etched microstructure of the cast alloys. The microstructure consists mainly of graphite nodules contained in a pearlitic-ferritic matrix. The presence of carbides that may correspond to Fe_3C, (Fe_2Mo) C, VC, and V_4C_3 (Han *et al.*, 2015a; Han *et al.*, 2015b) are also evident.

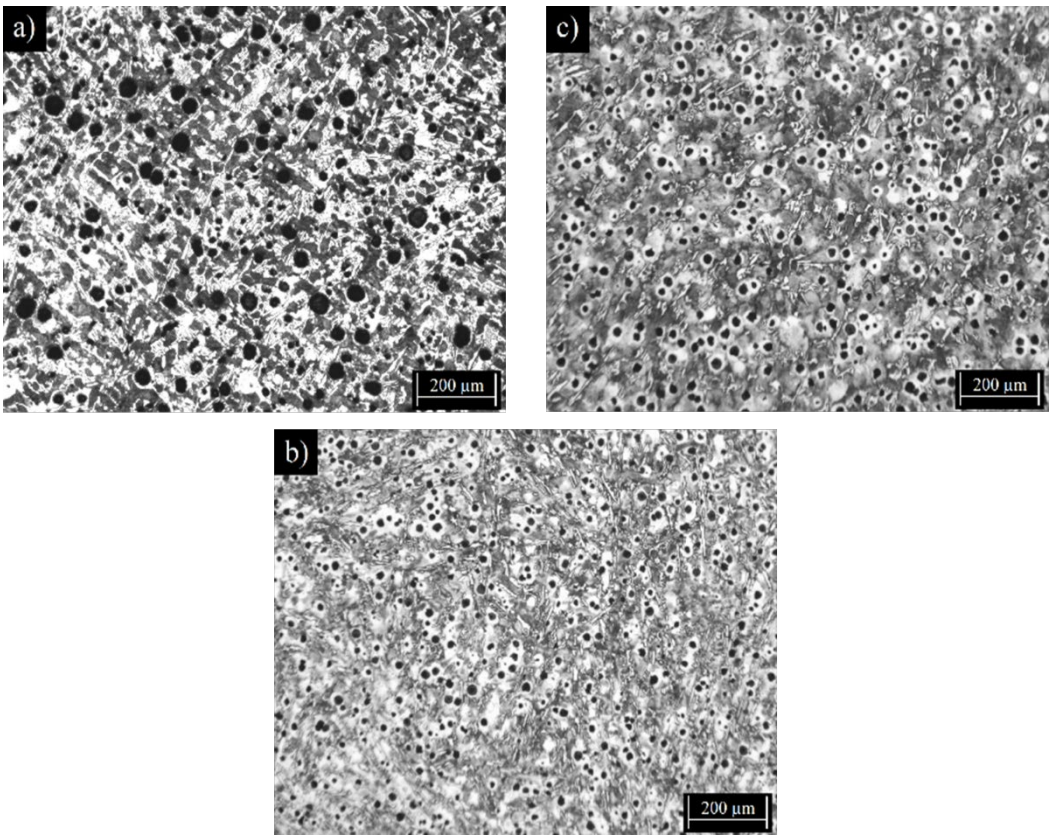

Figure 3. Etched microstructure of cast alloys: a) DI, b) DI-A, and c) DI-B.
Source: Authors' own elaboration.

The carbides were revealed by etching the as-cast samples with an ammonium persulfate solution, as can be observed in Figure 4. It was determined that cast alloys DI, DI-A, and DI-B contain volume fractions (vol.%) of carbides of 15.53, 3.09, and 2.05, respectively.

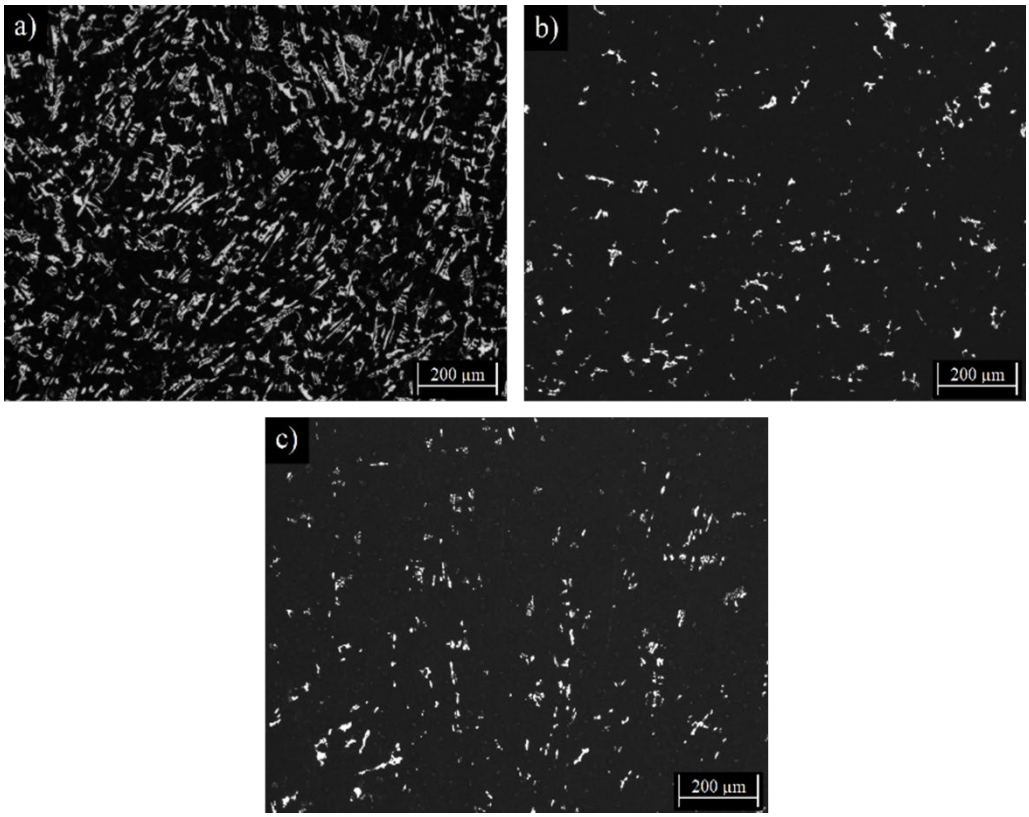

Figure 4. Etched microstructure with ammonium persulfate reveals the carbides phase (white regions) of cast alloys: a) DI, b) DI-A, and c) DI-B. Source: Authors' own elaboration.

The sample identified as DI for the unalloyed ductile iron shows a higher cementite formation. The thin thickness used (4.23 mm) in the as-cast plate increases the undercooling tendency and promotes metastable eutectic cementite formation. In this case, for the hypo-eutectic chemical composition (CE = 4.24) and the cooling rates imposed by the thin thickness evaluated, the cementite formation was unavoidable for the sample identified as DI. It is recommended (Ruxanda *et al.*, 2001; SORELMETALS, 1990) an equivalent carbon in the range of 4.3 to 4.6 to avoid carbide formation in thin section castings. The samples identified as DI-A and DI-B show a lower amount of carbides than sample DI. This is attributed to the higher carbon equivalent hypereutectic cast irons with carbides that may correspond to $(Fe_2Mo)C$ (Han *et al.*, 2015b), and VC and V_4C_3 types (Han *et al.*, 2015a) that may correspond to the DI-A and DI-B, respectively.

Table 3 shows nodule count, average nodule size, and the volume fraction of phases formed in the ductile irons produced. A higher nodule count with low nodule size was obtained for the ductile irons alloyed with V and V-Mo, while the unalloyed ductile iron shows the lowest nodule count with a large nodule size. The difference in the nodule count for the ductile irons produced is attributed to the effect of the percentage of carbon equivalent (%CE). When the percentage of carbon equivalent is increased, the nodule count is also increased, reaching a maximum value at CE = 4.61, while the nodule size shows the opposite behavior (Fatahalla *et al.*, 1996). According to the results in Tables 2 and 3, the DI-B shows the highest %CE, with the highest nodule count and the lowest nodule size. Pearlite is the primary microconstituent formed in the three cast ductile irons with the highest amount reported for the DI-B sample.

Table 3. Distribution of graphite and volume fraction of phases in the as-cast ductile irons.

Parameter	Cast alloy		
	DI	DI-A	DI-B
Nodule count (nod mm^{-2})	218	260.48	348.95
Average nodule size (μm)	28.42	14.6	14.3
Graphite (vol. %)	14.05	10.02	13.04
Ferrite (vol. %)	9.55	28.27	18.93
Pearlite (vol. %)	60.84	58.6	65.99
Carbides (vol. %)	15.53	3.09	2.01

Source: Authors' own elaboration.

The microstructure of the samples which were austenitized at 950 °C for 1 h and then austempered at 300 °C for 1 h are shown in Figure 5.

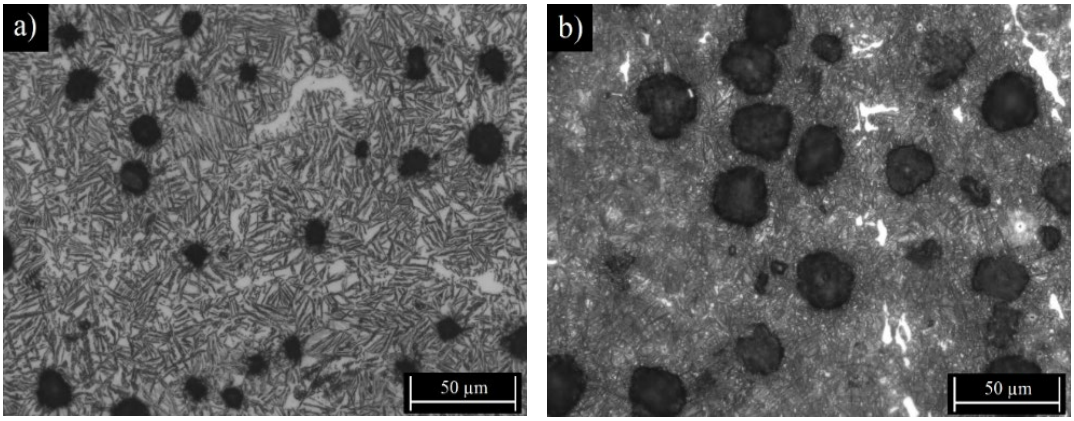

Figure 5. Etched microstructure of the austempered ductile irons of cast alloys: a) ADI-A and b) ADI-B.
Source: Authors' own elaboration.

The microstructures consist mainly of acicular ferrite in a stabilized high carbon austenite matrix (ausferrite microstructure), carbide, and nodular graphite. It is observed that the nodular graphite is dispersed in the microstructure. In spite that the austempering heat treatment was carried out under the same parameters, it is evident that the microstructure of Figure 5a corresponding to the ADI alloyed with vanadium presents an upper ausferritic microstructure consisting of broad ferrite needles. By contrast, the ADI alloyed with vanadium and molybdenum (Figure 5b) shows a lower ausferritic microstructure with very fine needles of ferrite. The addition of vanadium can refine grains effectively and promote the formation of acicular ferrite (Han *et al.*, 2015a; He & Edmonds, 2002). It is known that molybdenum can distribute both in acicular ferrite and carbide. During the austenitization process, the molybdenum in the austenite decreases the diffusion rate of carbon, and the discrete distribution of carbides has a pinning effect on grain growth. The combined effect of vanadium and molybdenum as carbide formers in the sample ADI-B accelerate the nucleation of acicular ferrite and refine the acicular ferrite grains, as can be observed in Figure 5b.

The potentiodynamic polarization curves for DI, DI-A, and DI-B obtained in 0.5 M of NaCl, 0.5 M NaOH, and 0.5 M H_2SO_4 solutions are shown in Figures 6, 7, and 8, respectively.

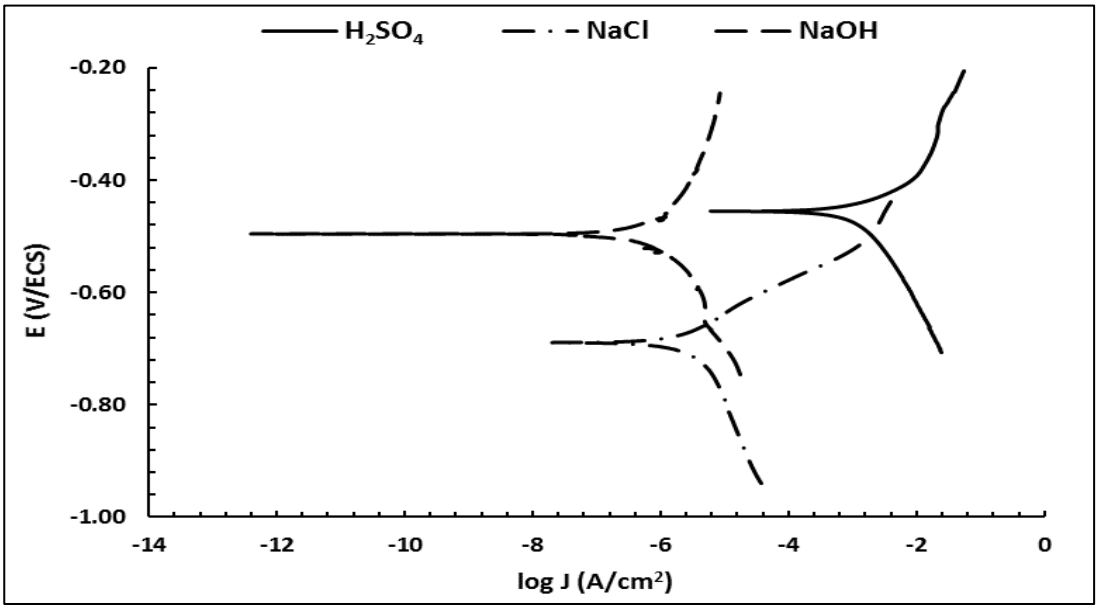

Figure 6. Polarization curves of the ductile iron (DI) in 0.5 M of H_2SO_4, 0.5 M NaCl, and 0.5 M NaOH solutions.
Source: Authors' own elaboration.

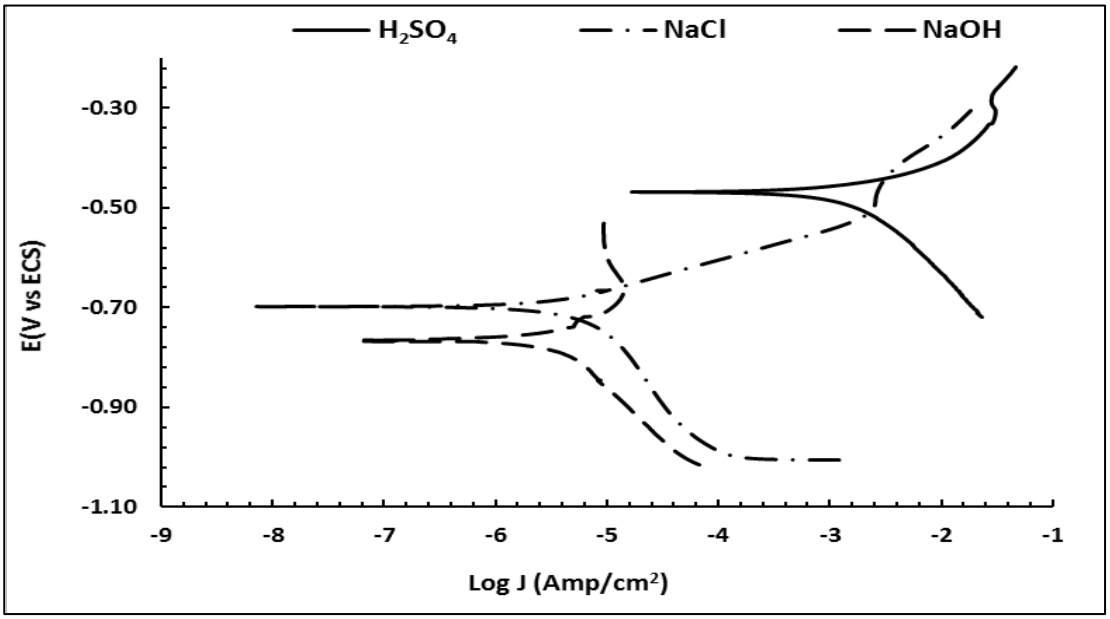

Figure 7. Polarization curves of the ductile iron (DI-A) in 0.5 M of H_2SO_4, 0.5 M NaCl, and 0.5 M NaOH solutions.
Source: Authors' own elaboration.

ISSN online 2007-9621

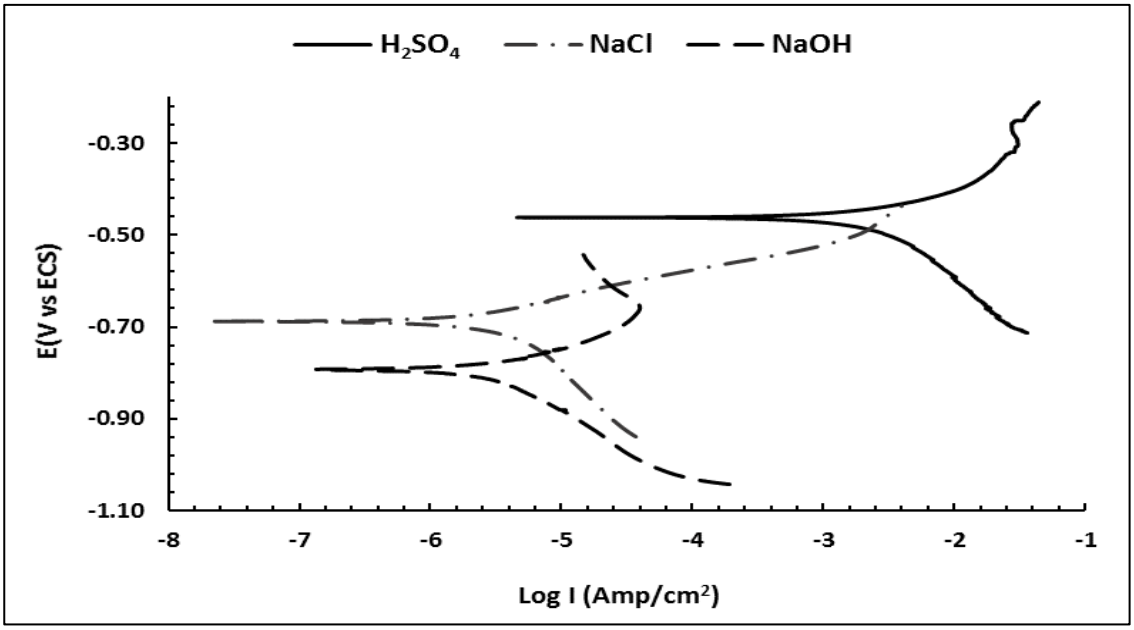

Figure 8. Polarization curves of the ductile iron (DI-B) in 0.5 M of H_2SO_4, 0.5 M NaCl, and 0.5 M NaOH solutions.
Source: Authors' own elaboration.

The corrosion potential and corrosion current density are extracted from the polarization curves by fitting the polarization curve. The corrosion current density and the corrosion potential reflect the corrosion resistance of the ductile iron in the environment evaluated. As the corrosion current increases, the rate of corrosion becomes faster, while higher corrosion resistance is indicated by a small corrosion current (Gollapudi, 2012; Stern & Geary, 1957). Table 4 shows the corrosion potential and the corrosion current of the ductile irons evaluated in different corrosive media.

Table 4. Corrosion potential and corrosion current density of the ductile irons and austempered ductile irons.

Corrosive media (0.5 M)	Sample	Corrosion potential (V vs SCE)	Corrosion current density (A cm^{-2})
H_2SO_4	DI	-0.453	7.11×10^{-4}
	DI-A	-0.460	1.38×10^{-3}
	DI-B	-0.461	1.09×10^{-3}
	ADI-A	-0.203	3.32×10^{-4}
	ADI-B	-0.505	8.71×10^{-4}
NaCl	DI	-0.675	2.53×10^{-6}
	DI-A	-0.666	3.75×10^{-6}
	DI-B	-0.688	2.64×10^{-6}
	ADI-A	-0.494	4.012×10^{-6}
	ADI-B	-0.464	1.99×10^{-6}
NaOH	DI	-0.499	6.31×10^{-7}
	DI-A	-0.795	2.67×10^{-6}
	DI-B	-0.758	2.34×10^{-6}
	ADI-A	-0.779	6.96×10^{-6}
	ADI-B	-0.314	5.518×10^{-7}

Source: Authors' own elaboration.

The potentiodynamic polarization results for ductile irons are reported in Figures 6 to 8 and Table 4. It is observed that DI has the lowest current density for the three corrosive media evaluated compared to the DI-A and DI-B samples, which means that the DI sample has the highest corrosion resistance. Considering the microstructural evaluation observed in Figures 2 to 4 and Table 3, the DI sample shows coarse graphite nodules, while the vanadium and molybdenum addition for DI-A and DI-B samples promotes a refined microstructure and an increase in the nodule count surrounded by ferrite and fine pearlite. This promotes a decrease in corrosion resistance due to the fact that corrosion is promoted by the galvanic graphite-ferrite pair (known as graphitic corrosion) (Logan *et al.*, 2014; Winston & Uhlig, 2008).

However, it must be considered that the DI sample presents few graphite nodules surrounded by ferrite, and the microstructure etched with ammonium persulfate reveals that DI contains a high amount of carbides compared to the DI-A and DI-B samples (Table 3 and Figure 4). The higher volume of carbides tends to increase the corrosion resistance (García *et al.*, 2019; ASM International, 1992; Sain *et al.*, 2016; Sutthiruangwong & Mori, 2005). Nevertheless, the presence of the carbide would not be beneficial for some applications because they cause fragility. In other words, if one takes into account that graphitic corrosion occurs mainly due to the potential difference between the graphite and the surrounding ferrite (Ahmad, 2006; ASM International, 1992; Logan *et al.*, 2014; Winston & Uhlig, 2008), then iron dissolution occurs from the following reactions:

$$Fe \rightarrow Fe^{2+} + 2e^{-} \quad \text{Anodic} \quad (1)$$

$$2H^{+} + 2e^{-} \rightarrow H_2 \quad \text{Cathodic} \quad (2)$$

ISSN online 2007-9621

In an acidic medium, iron corrosion is controlled by the cathodic reaction (Winston & Uhlig, 2008), increasing the rate of reaction when the pH decreases, which means that corrosion rate is determined by the rate of hydrogen evolution. This effect occurs for DI-A and DI-B heats, where the corrosion current increase in H_2SO_4.

In the case of an alkaline medium, the corrosion current decreases, which means that the corrosion rate decreases. This effect is observed in Figures 6, 7, and 8; this response is associated with the formation of a film of Fe(OH)x, which reduces the corrosion rate (Ahmad, 2006; Pourbaix, 1974; Winston & Uhlig, 2008).

Comparing the three media for DI-A and DI-B, and analyzing the corrosion currents shown in Table 4, it is observed that DI-B presents a lower corrosion current, which means that it has greater resistance to corrosion. According to the microstructural evaluation, both have the presence of graphite surrounded by ferrite, which generates the galvanic pair that promotes graphitic corrosion. However, because the phenomenon of corrosion is a process carried out on the metal contact surface, the advantage of DI-B iron is that the fine microstructure that produces smaller graphite nodules also reduces the presence of ferrite surrounding it (Figure 3c and Table 3). In addition, the presence of pearlite is increased, which results in a lower corrosion current in each medium concerning DI-A.

The potentiodynamic polarization curves for ADI-A and ADI-B are shown in Figures 9 and 10, respectively, obtained in 0.5 M of NaCl, 0.5 M NaOH, and 0.5 M H_2SO_4 solutions.

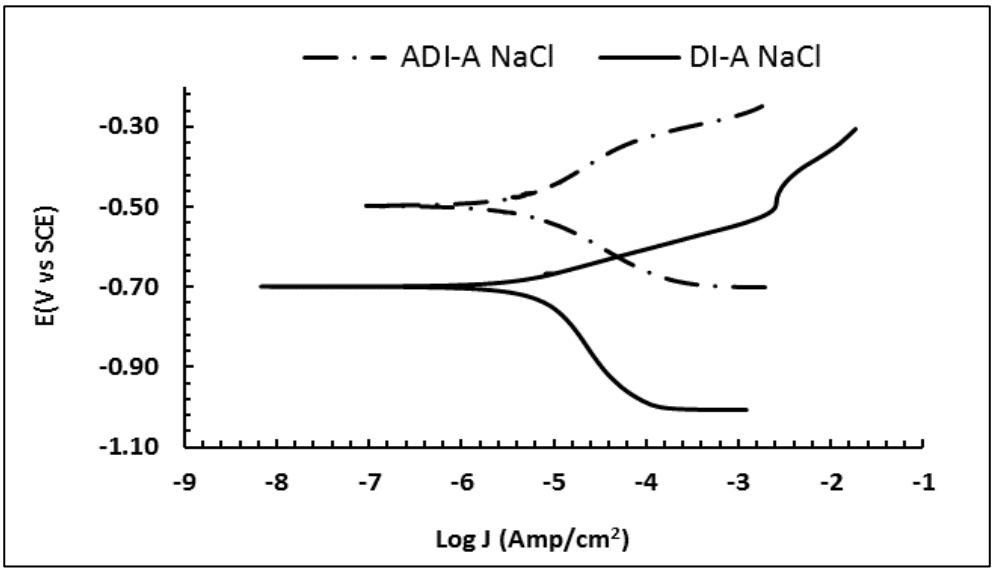

a)

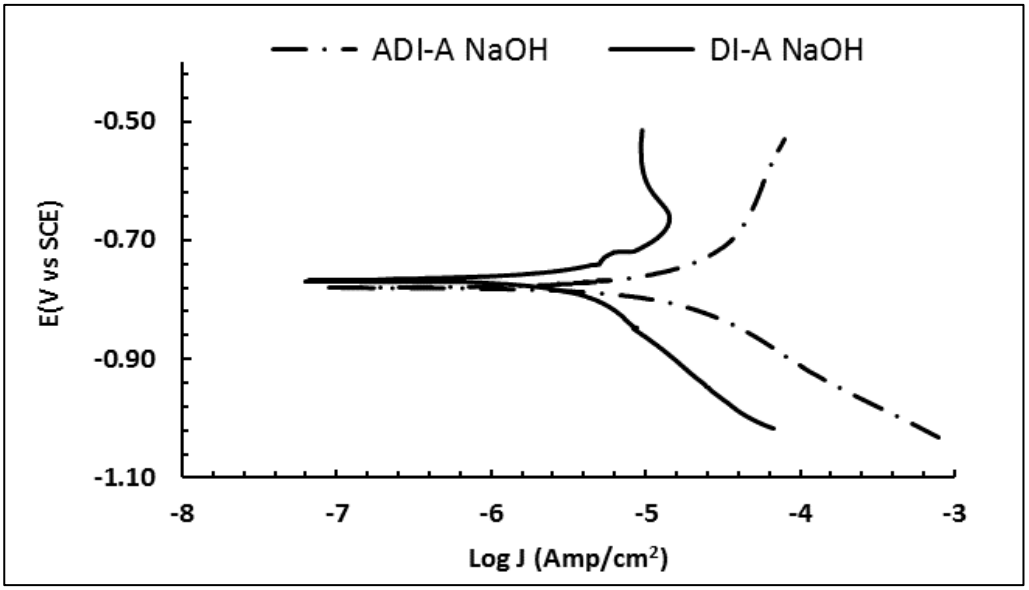

b)

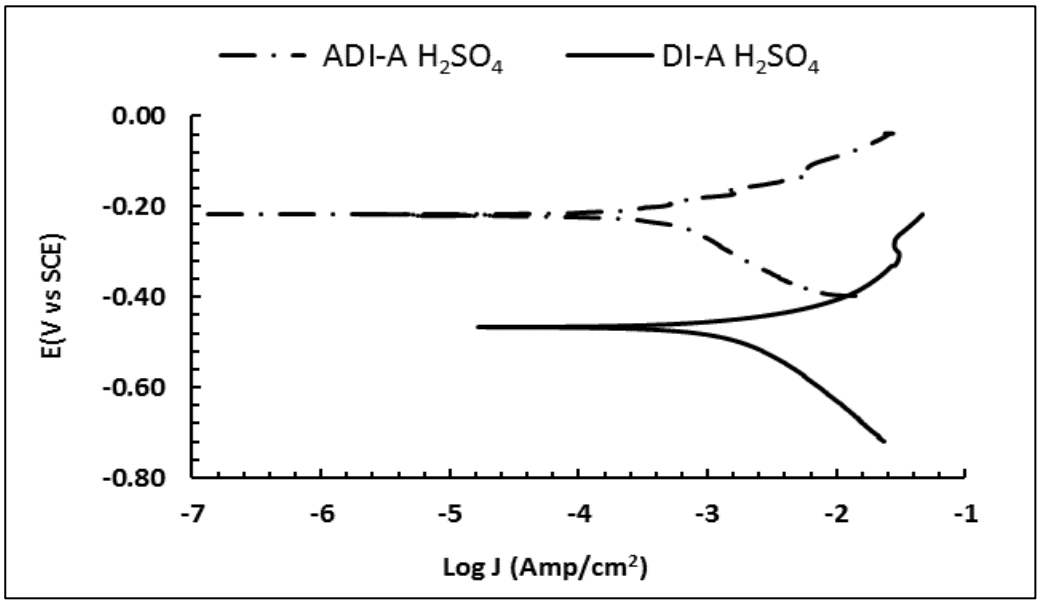

c)

Figure 9. Polarization curves of the DI-A and ADI-A in a) 0.5 M NaCl, b) 0.5 M NaOH, and c) 0.5 M H_2SO_4 solutions.
Source: Authors' own elaboration.

ISSN online 2007-9621

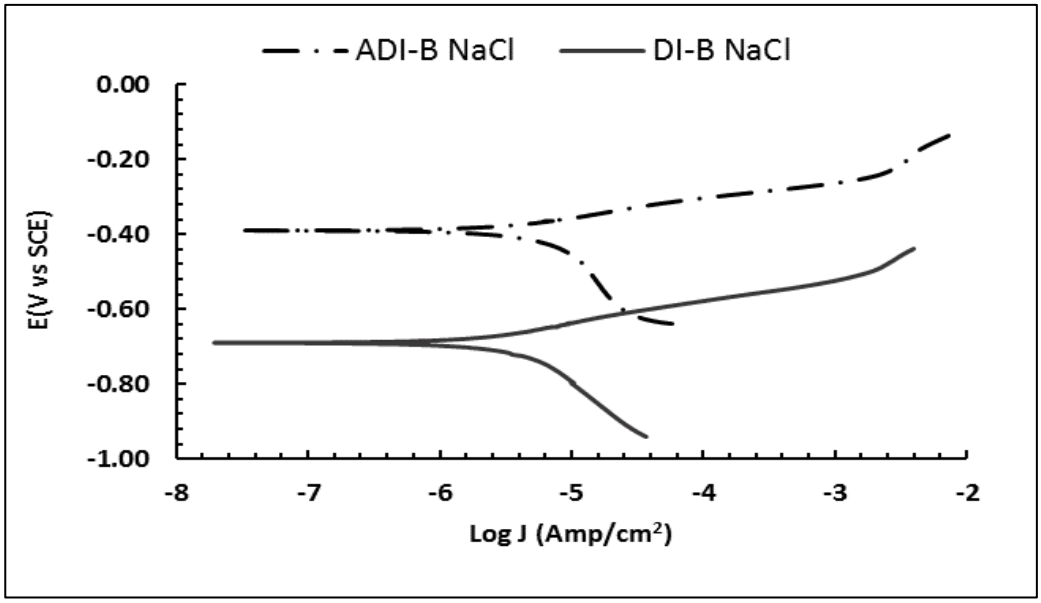

a)

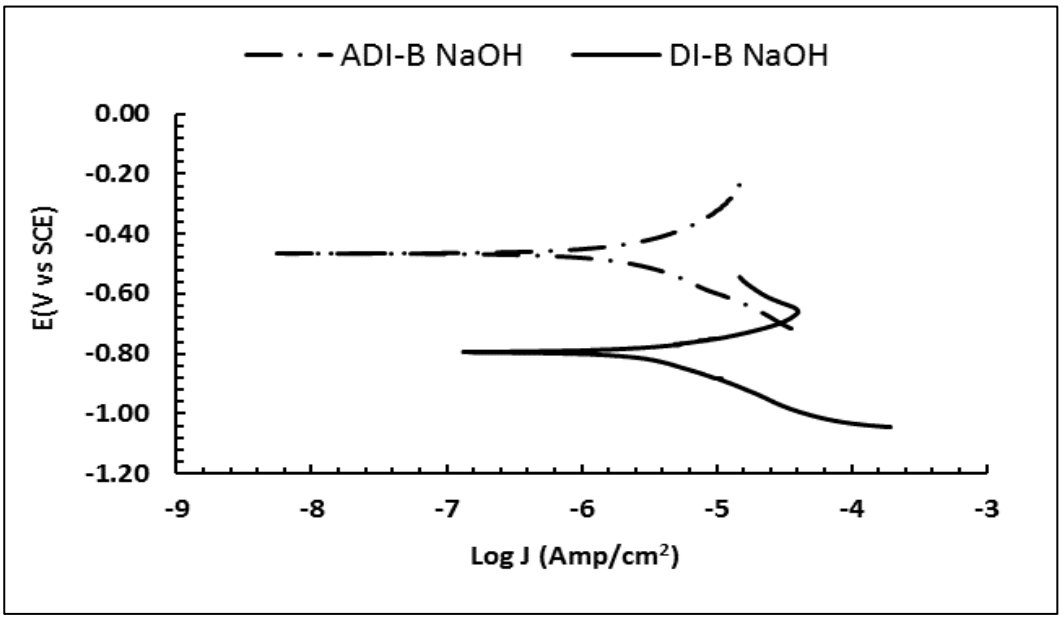

b)

ISSN online 2007-9621

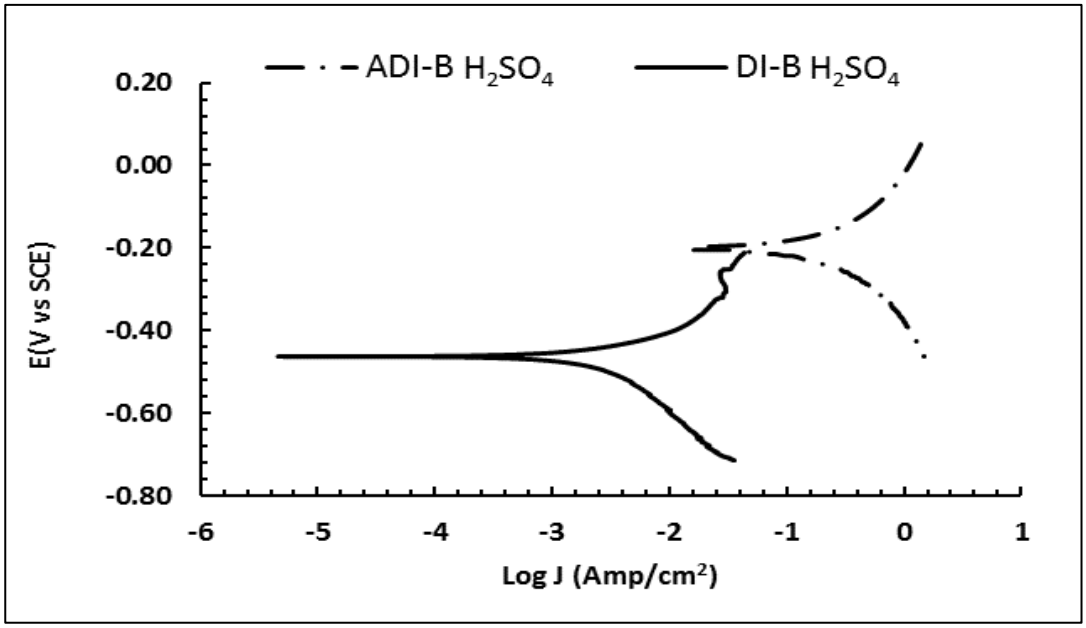

c)

Figure 10. Polarization curves of the DI-B and ADI-B in a) 0.5 M NaCl, b) 0.5 M NaOH, and c) 0.5 M H_2SO_4 solutions.
Source: Authors' own elaboration.

Table 4 and Figures 9 and 10 show the corrosion potential and the corrosion current density of the austempered ductile irons evaluated in different corrosive media. In a general way, the results show an increase in corrosion resistance compared to DI-A and DI-B versus ADI-A and ADI-B. However, where an increase in the corrosion current is observed, the corrosion potential tends to shift to positive values, indicating a lower tendency to corrode. This behavior is associated with the presence of a greater amount of acicular ferrite immersed in an austenite matrix, and the presence of these phases inhibit graphitic corrosion mentioned above (ASM International, 1992).

Among the three given aqueous solutions, the sulfuric acid solution is the most aggressive in reducing corrosion resistance. This is because as the pH decreases, the equilibrium potential of reaction 2 becomes nobler; therefore, the potential difference between reactions 1 and 2 becomes larger and, consequently, the corrosion current increases (Ahmad, 2006; ASM International, 1992; Winston & Uhlig, 2008).

Two dissolution mechanisms could occur in acid media (H_2SO_4); the first happens due to the sulfur ion, and the second one is caused by the oxygen (Banas *et al.*, 2007; Krawiec *et al.*, 2006). Both increase the dissolution rate of ductile irons and austempered ductile irons. Reactions 3 to 5 represent the dissolution mechanism in acid media (Krawiec *et al.*, 2006).

$$2Fe + 3H_2SO_4 \rightarrow Fe_2O_3 + 3SO_2 + 3H_2O \quad (3)$$

$$2Fe + 3H_2SO_4 \rightarrow 2FeOOH + 3SO_2 + 2H_2O \quad (4)$$

$$Fe + H_2SO_4 \rightarrow FeO + SO_2 + H_2O \quad (5)$$

Nonetheless, ADI-A and ADI-B show higher corrosion resistance than DI-A and DI-B and present more positive potentials attributed to the phase transformation obtained by heat treatment, which displaces the corrosion potential toward more positive or noble values.

The polarization curves evaluated in H_2SO_4 and NaCl media show an anodic current increase related to iron dissolution, unlike NaOH, where a passivation zone attributed the formation of FeOHx (Pourbaix, 1974). This zone is only observed in the ADI-A sample due to the potential scanning zone.

For the NaCl and NaOH corrosive media, reactions 6 and 7 occur (Logan *et al.*, 2014; Pierre, 2000).

$$2Fe \rightarrow 2Fe^{2+} + 4e \quad (6)$$

$$O_2 + 2H_2O + 4e^- \rightarrow 4OH \quad (7)$$

Hydroxyl ions (OH-) react with Fe^{2+} ion to form iron hydroxides according to the following reactions:

$$Fe^{2+} + 2OH^- \rightarrow Fe(OH)_2 \quad (8)$$

$$Fe(OH)_2 + OH^- \rightarrow Fe(OH)_3 + e \quad (9)$$

And the $Fe(OH)_3$ dehydration allows the formation of Fe_2O_3 according to reaction 10.

$$2Fe(OH)_3 \rightarrow Fe_2O_3 + 3H_2O$$

Reactions 6 to 10 show that the hydrogen generated will react with oxygen to form OH^- and then with iron, producing an iron hydroxide II, and finally iron hydroxide III. As the reaction mechanisms proceed, a hydroxide layer is formed, which causes that corrosion resistance depends on oxygen diffusion over this layer. In acid media, this layer gets dissolved, increasing the corrosion rate (Winston & Uhlig, 2008).

The austempered ductile irons produced show the presence of high carbon austenite and ausferrite. The dissolution of carbon in austenite will decrease the effect of a potential difference with graphite, decreasing the corrosion rate. The highest corrosion resistance in basic media is greater for the ADI-B. This behavior is due to the fine microstructure of ausferrite obtained by the combined addition of vanadium and molybdenum.

Conclusions

The unalloyed ductile iron shows a high cementite amount due to the cooling rates imposed by the thin thickness and the hypoeutectic chemical composition. This microstructure improves the corrosion resistance in acid media.

The microstructure of the heat-treated samples mainly consists of nodular graphite, acicular ferrite, austenite, and carbides. The acicular ferrite becomes thicker for the austempered ductile iron alloyed with vanadium, while the ADI alloyed with vanadium-molybdenum promotes the formation of a finer microstructure of acicular ferrite. This finer microstructure improves the corrosion resistance in 0.5 M NaCI and 0.5 M NaOH corrosive media.

In acid media (0.5 M H_2SO_4), the alloyed ADI showed a higher corrosion resistance compared to alloyed DI without heat treatment due to the phase transformation achieved by the heat treatment applied.

Acknowledgments

The authors wish to thank the institutions CONACYT, SNI, and SIP-Instituto Politécnico Nacional for their permanent assistance to the Process Metallurgy Group at ESIQIE-Metallurgy and Materials Department.

Referencias

Ahmad, Z. (2006). *Principles of corrosion engineering and corrosion control*. Elsevier Inc. Butterworth-Heinemann. doi: https://doi.org/10.1016/B978-0-7506-5924-6.X5000-4

Akinribide, O. J., Akinwamide, S. O., Ajibola, O. O., Obadale, B. A., Olusunle, S. O., & Olubambi, P. A. (2019). Corrosion behavior of ductile and austempered ductile cast iron in 0.01M and 0.05M NaCl Environments. *Procedia Manufacturing*, *30*, 167-172. doi: https://doi.org/10.1016/j.promfg.2019.02.024

Aristizabal, R., Foley, R., & Druschitz, A. (2012). Intercritically austenitized quenched and tempered ductile iron. *International Journal of Metalcasting, 6*, 7-14. doi: https://doi.org/10.1007/BF03355534

ASM Interntational. (1992). *Corrosion Volume 13: ASM metals handbook* (9th ed.). Gulf Professional Publishing. https://www.abebooks.com/9780872011540/Corrosion-Volume-ASM-Metals-Handbook-0872011542/plp

ASM International (2009). *Casting design and performance* (Technical book). ASM International. https://www.asminternational.org/documents/10192/3450755/05263G_Frontmatter.pdf/58851b1d-fece-4d01-ba2f-5ab5063c13c7

Banas, J., Lelek-Borkowska, U., Mazurkiewicz, B., & Solarski, W. (2007). Effect of CO_2 and H_2S on the composition and stability of passive film on iron alloys in geothermal water. *Electrochimica Acta, 52*(18), 5704-5714. doi: https://doi.org/10.1016/j.electacta.2007.01.086

Blackmore, P. A., & Harding R. A. (1984). The effects of metallurgical process variables on the properties of austempered ductile irons. *Journal Heat Treating, 3*, 310-325. doi: https://doi.org/10.1007/BF02833125

Brandenberg, K., Hayrynen, K. L., & Keough, J. R. (2001). Austempered gears and shafts: Tough solutions. *Gear Technology, 18*(2), 42-50. https://www.geartechnology.com/issues/0301x/brandenberg.pdf

Cheng-Hsun, H., & Ming-Li, C. (2010). Corrosion behavior of nickel alloyed and austempered ductile irons in 3.5% sodium chloride. *Corrosion Science, 52(9)*, 2945-2949. doi: https://doi.org/10.1016/j.corsci.2010.05.006

Fatahalla, N., Al Hakim, H. A., Abo-El-Ezz, A. A., & Mohamed M. (1996). Effect of the percentage carbon equivalent on the nodule characteristics, density and modulus of elasticity of ductile cast iron. *Journal Materials Science, 31*, 4933-4937. doi: https://doi.org/10.1007/BF00355883

García, J., Collado, V., Blomqvist, A., & Kaplan, B. (2019). Cemented carbide microstructures: A review. *International Journal of Refractory Metals and Hard Materials, 80*, 40-68. doi: https://doi.org/10.1016/j.ijrmhm.2018.12.004

Gollapudi, S. (2012). Grain size distribution effects on the corrosion behaviour of materials. *Corrosion Science, 62*, 90-94. doi : https://doi.org/10.1016/j.corsci.2012.04.040

Gonzaga, R. A., & Fernandez, J. (2005). Influence of an appropriate balance of the alloying elements on microstructure and on mechanical properties of nodular cast iron. *Journal of Materials Processing Technology, 162-163*, 293-297. doi: https://doi.org/10.1016/j.jmatprotec.2005.02.040

Han, Ch. F., Sun, Y. F., Wu, Y., & Ma, Y. H. (2015a). Effects of vanadium and austempering temperature on microstructure and properties of CADI. *Metallography, Microstructure, and Analysis, 4*, 135-145. doi: https://doi.org/10.1007/s13632-015-0197-1

Han, Ch. F., Wang, Q. Q., Sun, Y. F., & Li, J. (2015b). Effects of molybdenum on the wear resistance and corrosion resistance of carbidic austempered ductile iron. *Metallography, Microstructure, and Analysis, 4*, 298-304. doi: https://doi.org/10.1007/s13632-015-0215-3

He, K., & Edmonds, D. V. (2002). Formation of acicular ferrite and influence of vanadium alloying. *Materials Science Technology, 18*(3), 289-296. doi: https://doi.org/10.1179/026708301225000743

Hemanth, J. (2000). The solidification and corrosion behaviour of austempered chilled ductile iron. *Journal Materials Processing Technology, 101*(1-3), 159-166. doi: https://doi.org/10.1016/S0924-0136(00)00424-6

Krawiec, H., Lelito, J., Tyrala, E., & Banas, J. (2009). Relationships between microstructure and pitting corrosion of ADI in sodium chloride solution. *Journal of Solid State Electrochemistry, 13*, 935-942. doi: https://doi.org/10.1007/s10008-008-0636-x

Krawiec, H., Stypula, B., Stoch, J., & Mikolajczyk, M. (2006). Corrosion behaviour and structure of the surface layer formed on austempered ductile iron in concentrated sulphuric acid. *Corrosion Science, 48*(3), 595-607. doi: https://doi.org/10.1016/j.corsci.2005.02.019

Logan, R., Mulheron, M. J., Jesson, D. A., Smith, P. A., Evans, T. S., Clay-Michael, N., & Whiter, J. T. (2014). Graphitic corrosion of a cast iron trunk main: Implications for asset management. *WIT Transactions on The Built Environment, 139*, 411-422. doi: https://doi.org/10.2495/UW140351

Machado, H. D., Aristizabal-Sierra, R., Garcia-Moteo, C., & Toda-Caraballo I. (2020). Effect of the starting microstructure in the formation of austenite at the intercritical range in ductile iron alloyed with nickel and copper. *International Journal of Metalcasting, 14*, 836-845. doi: https://doi.org/10.1007/s40962-020-00450-1

McCafferty, E. (2005). Validation of corrosion rates measured by the Tafel extrapolation method. *Corrosion Science, 47*(12), 3202-3215. doi : https://doi.org/10.1016/j.corsci.2005.05.046

Minkoff, I. (1983). *The physical metallurgy of cast iron*. John Wiley and Sons Ltd.

Pedro, D. I., & Dommarco, R. C. (2019). Rolling contact fatigue resistance of Carbidic Austempered Ductile Iron (CADI). *Wear, 418-419*(15), 94-101. doi: https://doi.org/10.1016/j.wear.2018.11.005

Pierre, R. R. (2000). *Handbook of corrosion engineering.* McGraw-Hill Education. https://dl.icdst.org/pdfs/files/441d337b7410198db6d96e61a6716302.pdf

Pourbaix, M. (1974). *Atlas of electrochemical equilibria in aqueous solutions.* National Association of Corrosion Engineers. http://sunlight.caltech.edu/aic/pourbaix.pdf

Rajagopal, V., & Iwasaki I. (1992). Nature of corrosive and abrasive wear of chromium-bearing cast iron grinding media. *Corrosion, 48*(2), 132-139. doi: https://doi.org/10.5006/1.3299819

Roy, E. (1988). *Cast iron technology*. Butterworths-Heineman. https://www.sciencedirect.com/book/9780408015127/cast-iron-technology

Ruxanda, R., Beltran-Sanchez, L., Massone, J., & Stefanescu, D. M. (2001). On the eutectic solidification of spheroidal graphite iron– An experimental and mathematical modeling approach. *Transactions of American Foundry Society, 109*, 1037-1048. https://www.researchgate.net/publication/260106615_On_the_Eutectic_Solidification_of_Spheroidal_Graphite_Iron-_An_Experimental_and_Mathematical_Modeling_Approach

Sain, P. K., Sharma, C. P., & Bhargava, A. K. (2016). Influence of chromium and nickel variation on the microstructure, carbide morphology and corrosion behaviour in Fe–Mn–Cr–Cu based austenitic white irons. *International Journal of Cast Metals Research, 29*(6), 362-368. doi: https://doi.org/10.1080/13640461.2016.1151144

SORELMETALS. (1990). *Ductile iron data for design engineers*. Rio Tinto & Titanium Inc. https://www.ductile.org/Ductile-Iron-Data

Stern, M., & Geary, A. L. (1957). Electrochemical polarization: I. A theoretical analysis of the shape of polarization curves. *Journal of Electrochemical Society, 104*(1), 56-63. https://iopscience.iop.org/article/10.1149/1.2428496

Sutthiruangwong, S., & Mori, G. (2005). Influence of refractory metal carbide addition on corrosion properties of cemented carbides. *Materials and Manufacturing Processes, 20*(1), 47-56. doi: https://doi.org/10.1081/AMP-200041607

Winston, R., & Uhlig, H. H. (2008). *Corrosion and corrosion control: An introduction to corrosion science and engineering.* John Wiley and Sons, Inc. doi: https://doi.org/10.1002/9780470277270

Yufu, S., Sumeng, H., Zhiyun, X., Sansan, Y., Jingyu, Z., & Yezhe, L. (2012). Effects of nickel on low-temperature impact toughness and corrosion resistance of high-ductility ductile iron. *Materials & Design, 41*, 37-42. doi: https://doi.org/10.1016/j.matdes.2012.03.039